Electronic Supplementary Material (ESI) for Nanoscale.

Supporting information for:

Single molecule vs large area design of molecular electronic devices incorporating an efficient 2-aminepyridine double anchoring group

L. Herrer,[a,b,#] A. Ismael,[c,d,#] S. Martín,[a,e] D.C. Milan,[f] J. L. Serrano,[b,e,g*] R.J. Nichols,[e,*] C. Lambert,[c,*] and P. Cea[a,b,f*]

[a] Departamento de Química Física, Facultad de Ciencias, Universidad de Zaragoza, 50009, Zaragoza, Spain.

[b] Instituto de Nanociencia de Aragón (INA) and Laboratorio de Microscopias Avanzadas (LMA), Edificio I+D Campus Río Ebro, Universidad de Zaragoza, C/Mariano Esquillor, s/n, 50018 Zaragoza, Spain.

[c] Department of Physics, University of Lancaster, Lancaster, LA1 4YB, United Kingdom.

[d] Department of Physics, College of Education for Pure Science, Tikrit University, Tikrit, Iraq.

[e] Department of Chemistry, University of Liverpool, Crown Street, Liverpool, L69 7ZD, United Kingdom.

[f] Instituto de Ciencias de Materiales de Aragón (ICMA), Universidad de Zaragoza-CSIC, 50009 Zaragoza, Spain.

[g] Departamento de Química Orgánica, Facultad de Ciencias, Universidad de Zaragoza, 50009, Zaragoza, Spain.

#: these authors contributed equally to this work.

Corresponding authors:

Jose Luis Serrano: joseluis@unizar.es

Richard J. Nichols: R.J.Nichols@liverpool.ac.uk

Colin Lambert: c.lambert@lancaster.ac.uk

Pilar Cea: pilarcea@unizar.es

Table of Contents

A. Synthesis of compound 1 and spectra. ^{1}H NMR, ^{13}C NMR.

Compound **1** has been synthesized through a three-stages pathway, Figure S1. For the first stage, commercial 4-iodopicolinic acid (1.00 g, 4 mmol) was dissolved in 6 mL *tert*-butanol together with 6 mL of toluene and 1.4 mL of dry trimethylamine (TEA). The mixture was stirred under inert conditions for 15 minutes and then diphenyl phosphorazidate, DPPA, (1.1 mL, 5.1 mmol) was slowly added to the reaction flask. The ensemble was placed at 100 °C and under stirring for 24 h. Solvent was removed through the vacuum pump, and the solid extracted in ethyl acetate-water. The organic phase was washed with aqueous $NaHCO_3$ (1x) and brine (1x), dried with $MgSO_4$ and filtered. The crude product was purified by column chromatography on silica gel using a mixture of hexane:ethyl acetate (19:1) as eluent to obtain the pure compound tert-butyl (4-iodopyridin-2-yl)carbamate. Yield: 54%. ^{1}H NMR: (400 MHz, $CDCl_3$) δ 8.55 (s, 1H), 8.20 (s, 1H), 7.85 (s, 1H), 7.39 (s, 1H), 1.53 (s, 9H).

Step 2 is based on the Sonogashira coupling reaction. Tert-butyl (4-iodopyridin-2-yl)carbamate (0.67g, 2.1 mmol), $Pd(PPh_3)_4$ (10 % mol) and CuI (10 % mol), were placed into a schlenk, *A*. Concurrently, 1,4-diethynylbenzene (0.124 g, 0.985 mmol) was dissolved in dry TEA, 4 mL. The reaction flask was degassed by three pump-thaw cycles refilled with inert atmosphere. The content was cannulated to the schlenk *A*, and other 8 mL of dry TEA were added. After ensuring inert conditions, the reaction flask was maintained at 60 °C for 20 h under stirring. Solvent was removed trought the vacuum pump, and the crude solid was washed by a mild process in water, brine, THF, NH_4OH (aq.), diethylether and hexane, obtaining a rather insoluble off-white powder named compound *A* di-tert-butyl (4,4'-(1,4-phenylenebis(ethyne-2,1-diyl))bis(pyridine-4,2-diyl))dicarbamate). Yield: 83%. This intermediate was characterized by IR (KBr, υ, cm^{-1}): 3197 (-NH-), 2975 (C-H, $-CH_3$), 2218 (-C≡C-), 1728 (-COO-).

To obtain compound **1**, compound *A* (0.421 g) was dissolved in 5 mL of trifluoroacetic acid and maintained for 1 h at room temperature under stirring. 20 mL of Milli-Q water were gradually added to the reaction flask, and the solution was neutralized by aqueous $NaHCO_3$. The mixture was extracted with ethyl acetate and the organic phase was washed with water, saturated aqueous brine solution, and evaporated to dryness to afford the product. Finally, the obtained whitish powder was triturated in a filter plate with Milli-Q water and hexane to obtain 0.174 g. Yield: 69%. ^{1}H NMR (500 MHz, DMSO-d_6, δ (ppm)): 7.94 (d, J = 4.7 Hz, 2H), 7.62 (s, 4H), 6.60 (d, J = 4.6 Hz, 2H), 6.56 (s, 2H), 6.12 (s, 4H).

^{13}C NMR (125 MHz, DMSO-d_6, δ (ppm)): 159.89, 148.41, 131.97, 130.24, 122.28, 113.26, 109.41, 90.59, 89.82. EM (m/z): 311.4 (M+1).

Figure S1 summarizes the synthetic protocol followed in this contribution. Steps 1 and 3 have been adapted from previously described procedures.[1]

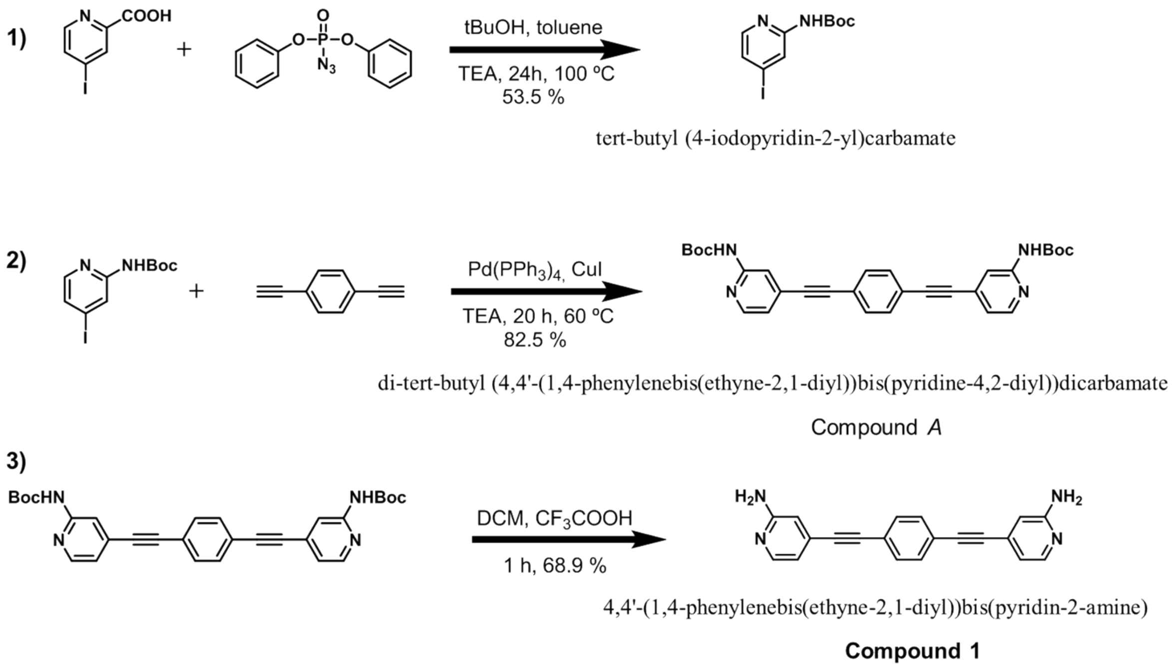

Figure S1. Three-stages synthetic scheme to obtain compound **1**.

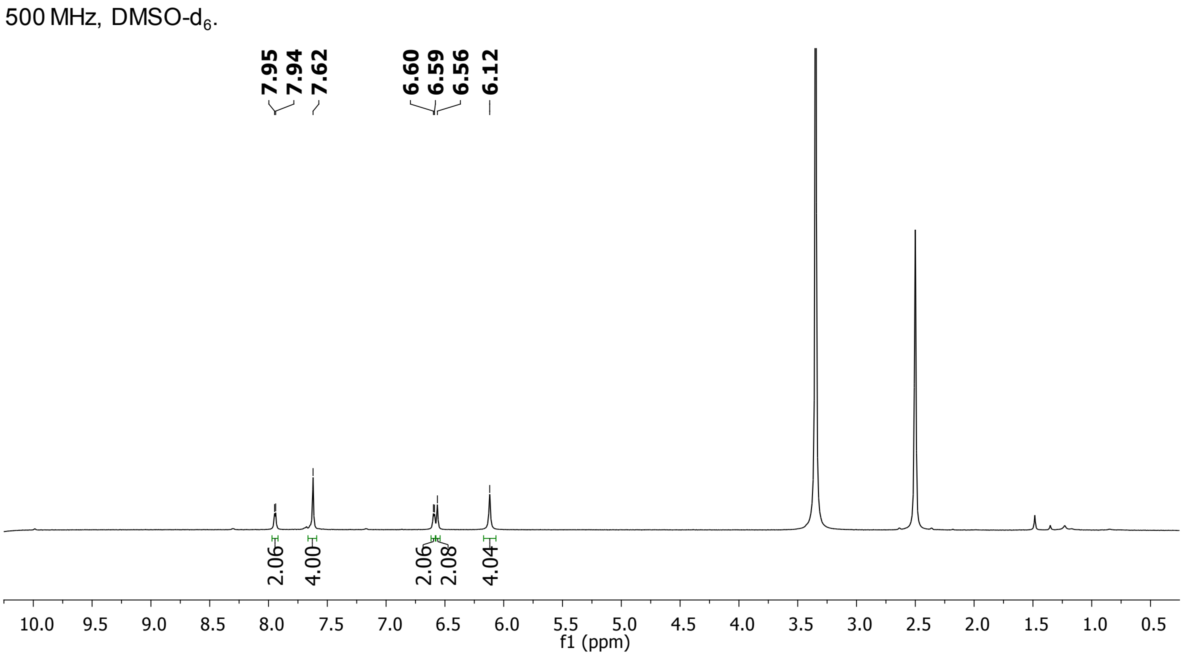

Figure S2. ^{1}H NMR spectrum of compound **1.**

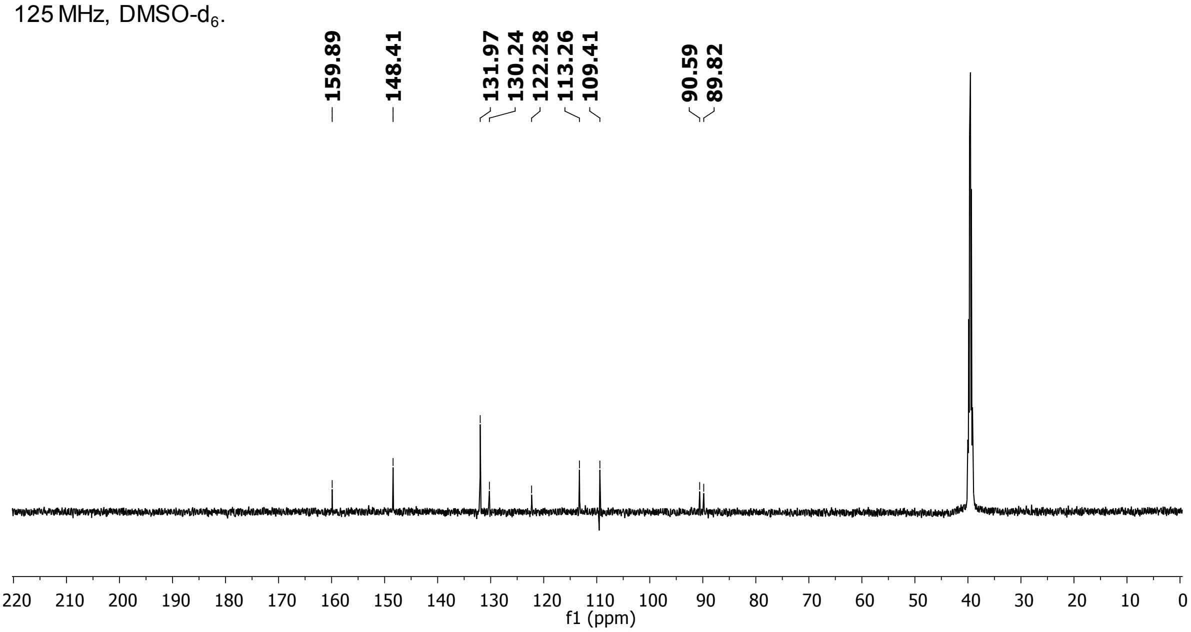

Figure S3. ^{13}C NMR spectrum of compound **1.**

B. Langmuir-Blodgett (LB) monolayer fabrication and characterization.

B.1. Langmuir films.

A 2.5x10^{-5} M solution of compound **1** in DMSO:CHCl$_3$ in the 1:4 ratio was used as the spreading solution on the water surface to fabricate the Langmuir films. This working concentration ensures the absence of molecular aggregates in the solution with the compliance of the Lambert-Beer law as evidenced in Figures S4.a and S4.b. The solution was spread onto the water surface of a NIMA 702 BAM (700 x 100 mm^2) trough with an initial area per molecule of 20 nm^2·molecule^{-1}. A lateral mechanical compression of the film was applied with the aid of a mobile barrier swept at a speed of 12 mm·min^{-1}. Under these experimental conditions reproducible surface pressure vs. area per molecule (*π-A*) isotherms recorded at 20 ºC were obtained (Figure S4.c).

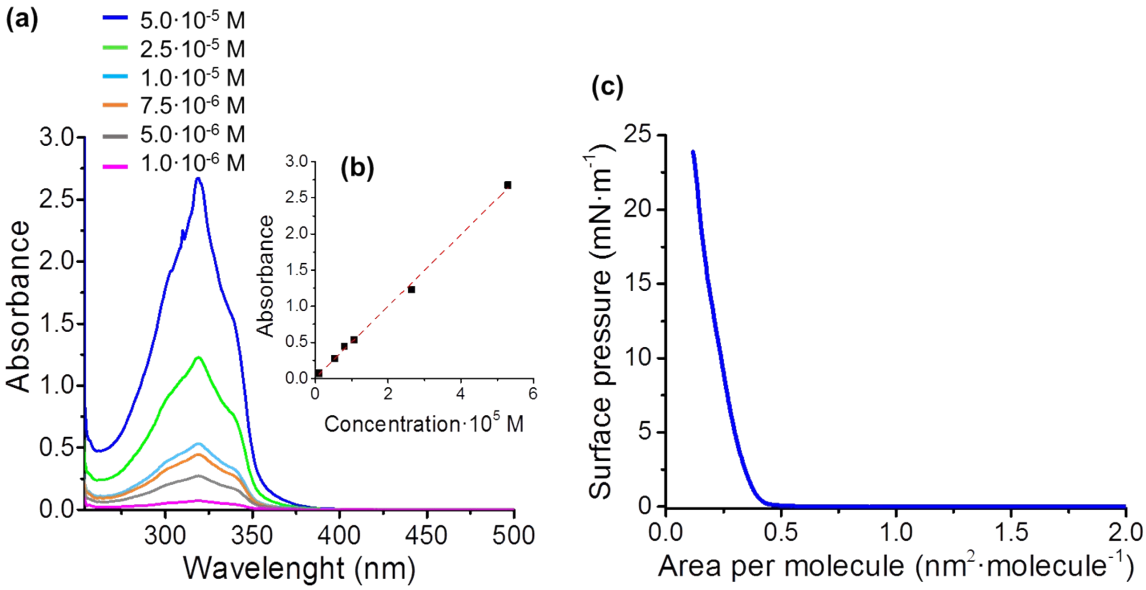

Figure S4. (a) UV-vis spectra of compound **1** in DMSO:CHCl$_3$ 1:4 at the indicated concentrations. **(b)** Absorbance at 319 nm vs. concentration, and linear fitting of the experimental values from which the molar absorptivity of compound **1** is obtained: 49500 L·mol^{-1}·cm^{-1}. **(c)** Representative *π-A* isotherm of compound **1** on water at 20 ºC.

Langmuir films were transferred onto solid substrates at a surface pressure of 8 mN·m^{-1} (0.26 nm^2·molecule^{-1}), and a dipping speed of 2 mm·min^{-1}. The as obtained LB monolayers were characterized by AFM, which evidences highly homogeneous and well-packed LB films of compound **1** as illustrated in Figure S5.

B.2. Thickness of the LB monolayers.

The thickness of the LB monolayer incorporating compound **1** has been determined by scratching the sample with the AFM tip. A height analysis of the scratched and a surrounding area with and without the organic film, respectively, allows for a thickness value of 1.6 ± 0.1 nm, as shown in Figures S5.c and S5.d.

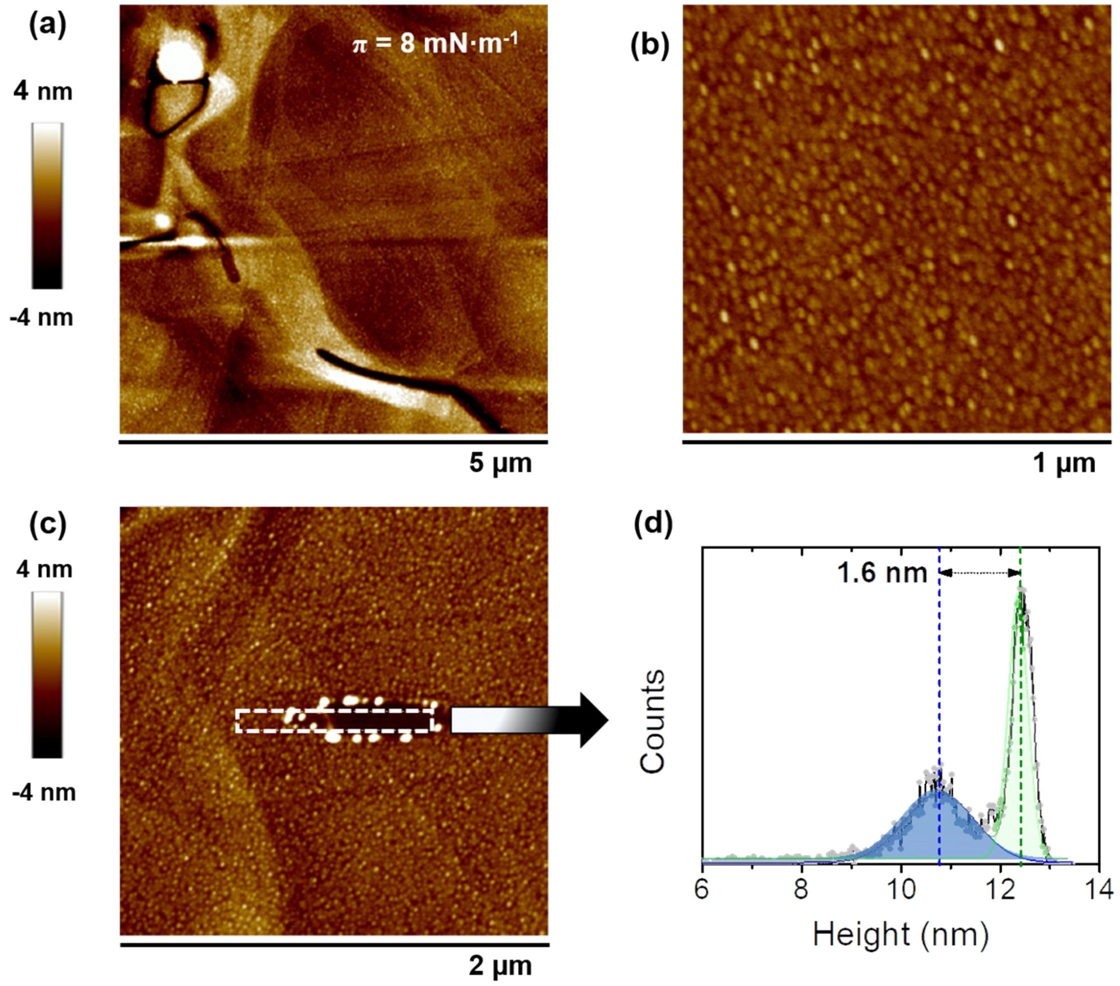

Figure S5. a) and **b)** 5x5 μm^2 and 1x1 μm^2 representative AFM images of LB monolayers transferred at 8 $mN \cdot m^{-1}$, respectively. **c)** Representative scratched surface with the AFM tip to estimate the monolayer thickness at 8 $mN \cdot m^{-1}$. **d)** Height profile across the scratched area, dotted white rectangle indicated at c).

The thickness of the LB film of compound **1** on gold substrates was also estimated from XPS experiments using the attenuation of the intensity of Au 4f signal from the gold substrate (Figure S6). The following formula was employed here: $I_{LB}\ film = I_{substrate}\ exp(-d/\lambda sin\theta)$. Using this equation a thickness value of the film of 1.6 ± 0.1 nm was obtained. In this equation d is the thickness of the film, θ is the photoelectron take-off angle, λ is the effective attenuation length of the photoelectron which is taken as 4.2 ± 0.1 nm).[2] Finally, I_{LB} film and $I_{substrate}$ are the average of the intensities of the Au $4f_{5/2}$ and Au $4f_{7/2}$ peaks attenuated by the LB film and from bare gold, respectively, θ is the photoelectron take-off angle, and λ is the effective attenuation length of the photoelectron (4.2 ± 0.1 nm).[2]

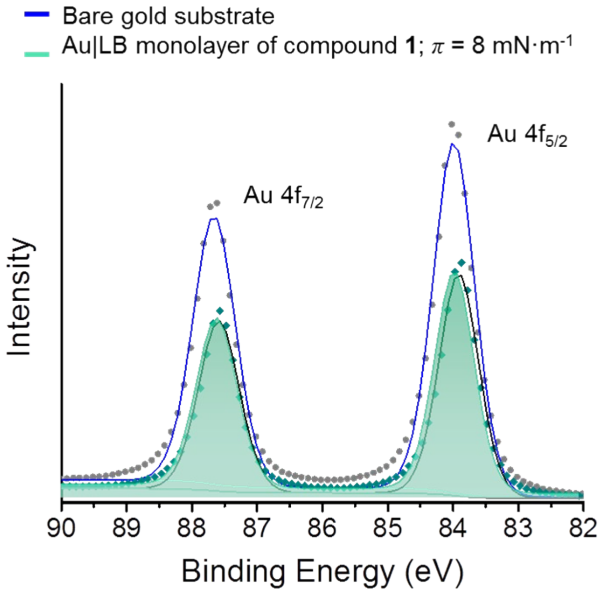

Figure S6. XPS spectra of Au 4f region for a bare gold substrate and for a LB monolayer of compound **1** transferred at 8 mN·m^{-1}.

C. Initial tip-substrate distance (s_0). Calibration for the $I(s)$ method, single molecule electrical measurements.

As previously reported the initial tip-substrate distance (s_0) is determined using a quantification of the current decay value , ($d\ln(I)/ ds$).[3] 20 $I(s)$ traces were recorded which featuring a monotonic exponential decay of the tunneling current. These traces were recorded with the following set-point parameters: I_0 = 30 nA and U_t = 0.3V, (Figure S7.a). These traces were then plotted as ln(I) vs. s (Figure S7.b) and this yielded an average slope of $d\ln(I)/ ds$ = 7.26 ± 0.44 nm^{-1}. At the beginning of each ln$I$ vs s trace there was a short non-linear region, which was omitted. This omitted region was attributed to an initial piezo delay resulting from inertia in the retraction process.

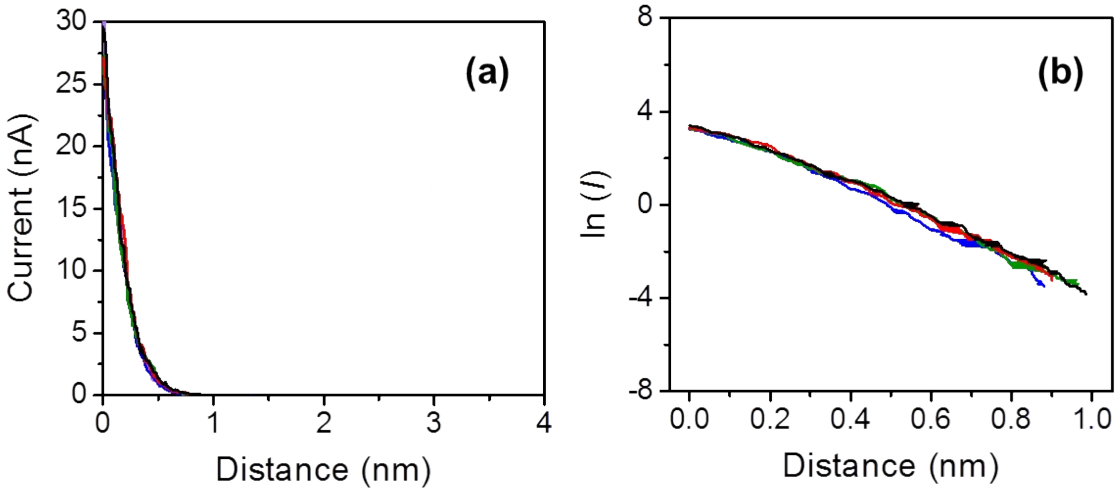

Figure S7. **(a)** A collection of overlaid $I(s)$ calibration curves recorded in mesytilene. **(b).** Examples of linear regions of ln I vs s plots used for the calibration of tip–substrate distance starting from the $I(s)$ calibration curves.

Equation 1 was used to determine the initial tip-substrate distance (s_0):

$$s_0 = \frac{ln\left(G_0 U_t / I_0\right)}{dln(I)/ds} \tag{1}$$

This equation uses the ($d\ln(I)/ds$) slope value combined with an extrapolation to G_0 ($G_0 = 2e^2/h = 77.5$ µS), which corresponds to extrapolating to the point where the STM tip would just touch the gold surface. This then provides the estimate of the tip-substrate distance for given set-point parameters. For the set-point parameters here and $d\ln(I)/ ds = 7.26 \pm 0.44$ nm^{-1} a value of $s_0 = 0.92$ nm is obtained.

D. Initial tip-substrate distance (s_0). Calibration for the *TTC* method, monolayer electrical measurements.

Calibration for positioning the STM probe at desired tip-substrate distance (s) under ambient air conditions have been carried in a similar manner to that explained in section C, obtaining an averaged slope ($d\ln(I)/ ds$) = 6.9 ± 1.3 nm^{-1}.

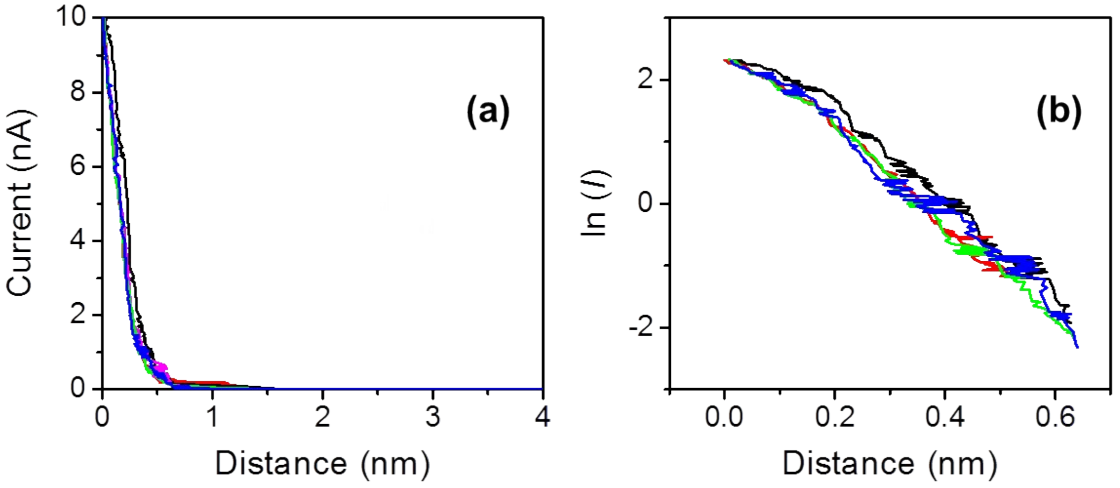

Figure S8. **(a)** Representative *I*(*s*) calibration curves recorded in ambient air. (**b)** Examples of regions of ln *I* vs *s* plots, used for calibration of the tip–substrate distance starting from the *I*(*s*) calibration curves.

D. Break-off distance.

The break-off distance is defined as the tip-substrate distance at which the molecular junction cleaves while the STM tip is being retracted in the single molecule measurements. Figure S9 shows the break-off distance for compound **1** corrected with the initial tip-substrate distance, s_0 = 0.92 nm, Figure S7.

The break-off distance obtained from the histogram (Figure S9) is 1.35 ± 0.1 nm. This value is shorter than the molecule length (1.8 nm), indicating that the molecule is not completely orthogonal to the surface of the substrate when the molecular junction breakage occurs.

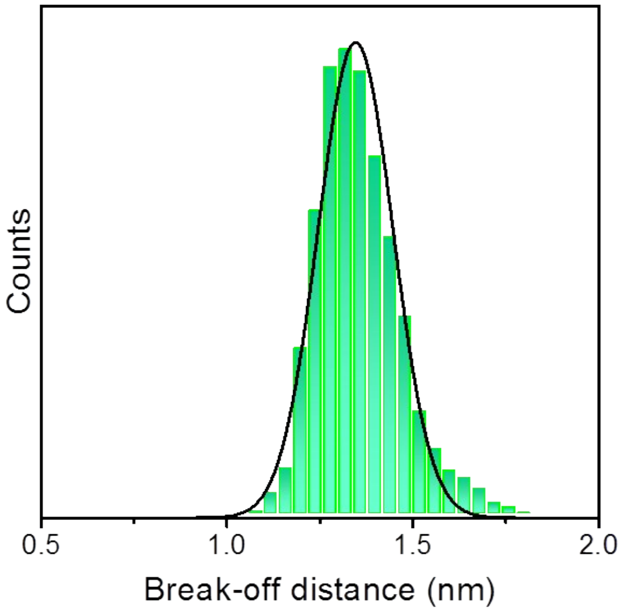

Figure S9. Break-off distance histogram.

E. Density Functional Theory (DFT) calculations.

E.1. Geometry of isolated isomers.

The DFT code (SIESTA) was used to obtain fully relaxed geometry of the isolated molecule (isomer-1 and isomer-2), as shown in Figure S10.

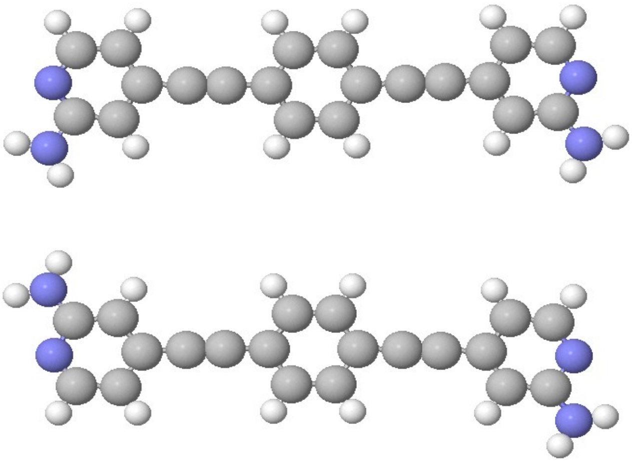

Figure S10. Fully relaxed isolated compound **1** in the two isomeric configurations considered in this contribution, i.e., isomer-1, *cis* configuration (top panel), and isomer-2, *trans* configuration (bottom panel).

E.2. Binding energy of isomer-1 and isomer-2 on gold.

To calculate the optimum binding distance for isomer-1 and isomer-2 when placed between two gold (111) surfaces, we used DFT and the counterpoise method, which removes basis set superposition errors (BSSE). The binding distance d is defined as the distance between the gold surface and the pyridine-N atom of the molecule. If isomer-1 or isomer-2 are defined as entity A and the gold electrodes as entity B, then the ground state energy of the total system is denoted as E_{AB}^{AB}. This parameter, E_{AB}^{AB}, is calculated using SIESTA with the parameters defined in the main text, but using a van der Waals[4] instead of LDA to describe the exchange correlation. Here the gold leads consist of 6 layers of 30 atoms. The energy of each monomer is then calculated in a fixed basis, which is achieved through the use of ghost atoms in SIESTA. Hence the energy of the individual molecule in the presence of the fixed basis is defined as E_{A}^{AB} and for the gold is E_{B}^{AB}. The binding energy of entity A to entity B is then calculated using the following equation:

$$Binding\ Energy = E_{AB}^{AB} - E_{A}^{AB} - E_{B}^{AB} \qquad (2)$$

The binding energy for isomer-1 as a function of molecule-contact distance is shown in the left panel in Figure S11. A schematic illustration of isomer 1, cis configuration, attached to a gold lead (N-Au contact) is shown in the right panel of Figure S11. Both isomers exhibit the same binding energy of approximately 0.6 eV to the gold electrode.

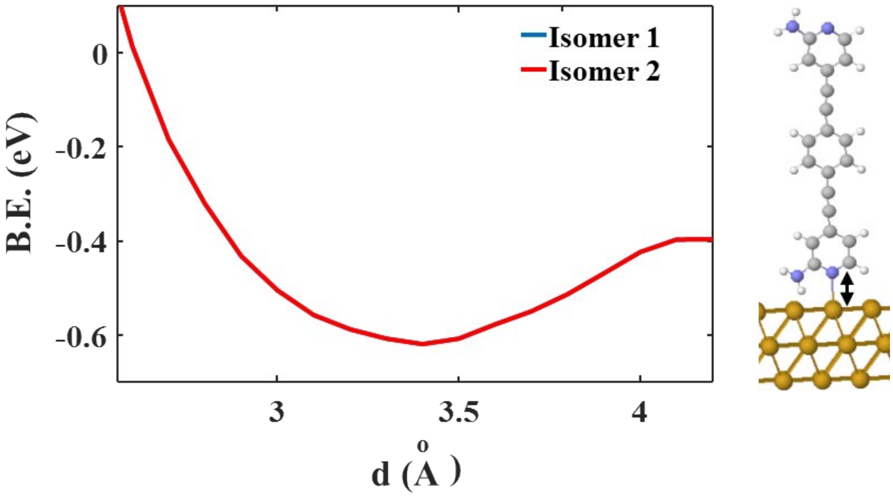

Figure S11. Left panel: Binding energy for each isomer as a function of molecule-contact distance (vdW). The equilibrium distance N-Au (i.e. the minimum of the binding energy curve) is found to be approximately 3.4 Å for both isomers. **Right panel**: Scheme of isomer 1, *cis* configuration, attached to gold leads (N-Au contact). Note that the two lines are identical and one is overlayed by the other and that is why the blue one cannot be seen.

E.3. Isomerisation of *cis* and *trans* isomers of compound 1.

To examine the energy barrier between the two isomers of compound **1** (cis and trans, Figure S12), the change in total energy due to the rotation of one of the terminal rings was calculated, while fixing the other ring as shown in the right panel of Figure S12.

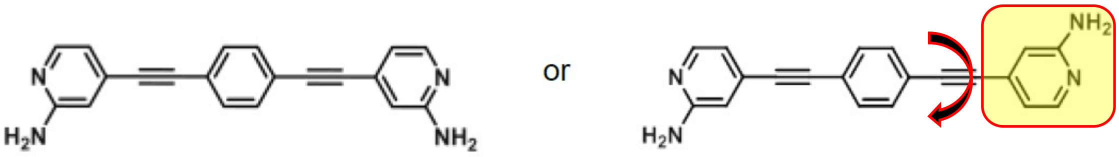

Figure S12. Two isomeric configurations of compound **1**: isomer-1 (*cis*, **left panel**) and isomer-2 (*trans*, **right panel**).

Figure S13 shows that the energy barrier is larger than k_BT at room temperature (25 meV). Figure S13 also indicates that the energy barrier is in the order of 60 meV and therefore the ring has two preferred orientations, but at room temperature there will be flipping between them.

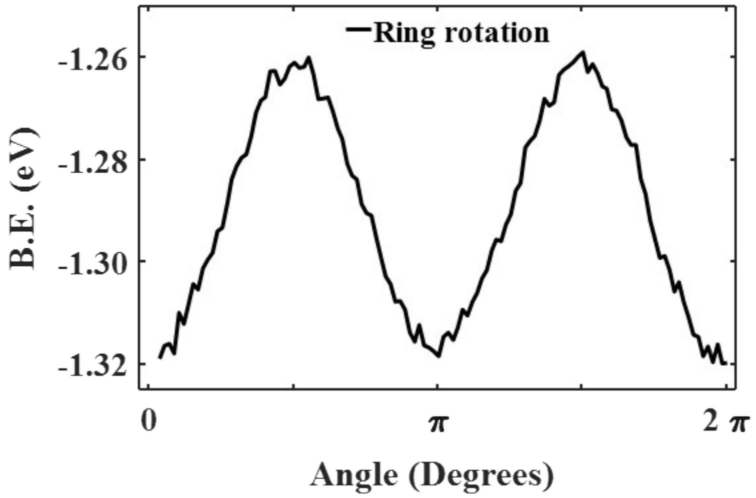

Figure S13. Binding energy as a function of rotation of one of the terminal rings of compound **1** (vdW).

E.4. Binding energy as a function of the tilt angle (*θ*).

In this section, we determine the preferred tilt angle θ of the molecules on a gold substrate as shown in Figure S14. The energy minimum in Figure S15 suggests that compound **1** prefers to tilt with an angle θ ranging from 29° to 42°.

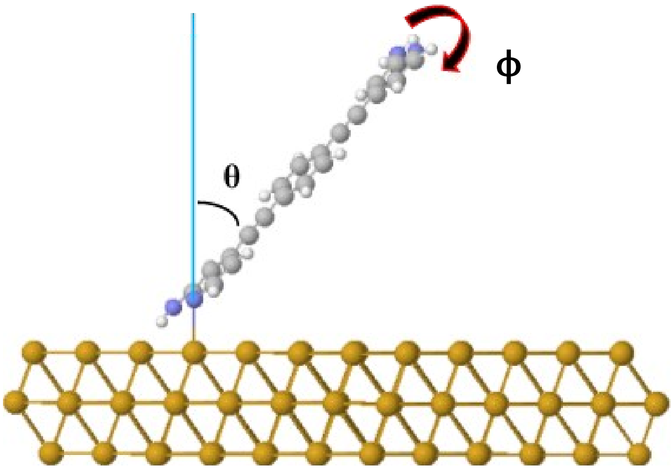

Figure S14. Cartoon showing the polar tilt angle θ and azimuthal angle ϕ of a molecule on a gold substrate.

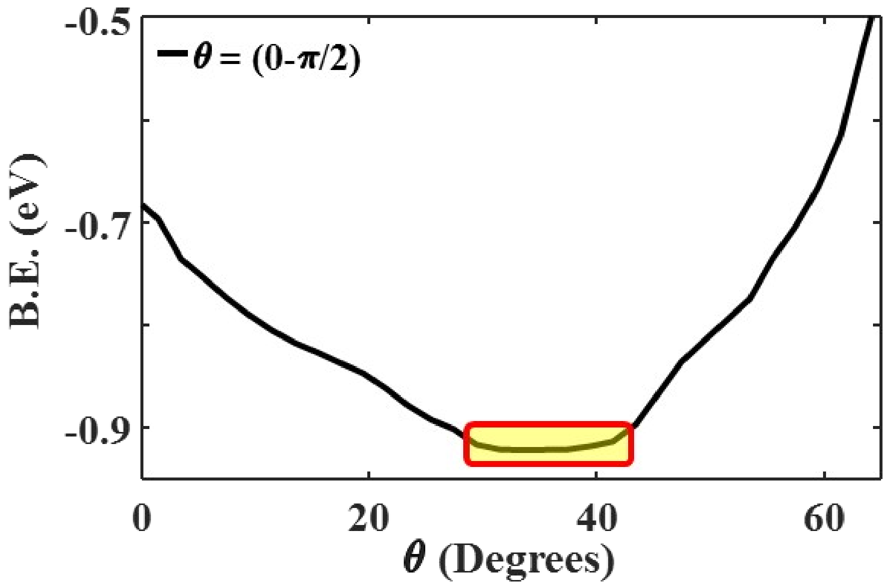

Figure S15. Binding energy as a function of the tilt angle for compound **1** (vdW). Binding energy calculations suggest the tilt angle to be in the 29.4 - 41.4° range and the experiment results from break-off junctions indicate a tilt angle of 40°.

E.5. Binding energy as a function of the of the azimuthal rotation angle (*ϕ*).

After finding the the optimum tilt angle, compound **1** was rotated around its long axis to determine whether this molecule prefers a specific azimuthal angle. The most energetically favorable binding distance indicates that the tilt angle *θ* is between 29° to 42°. Additionally, the most energetically favorable azimuthal angle, *ϕ*, is 0° (Figure S16).

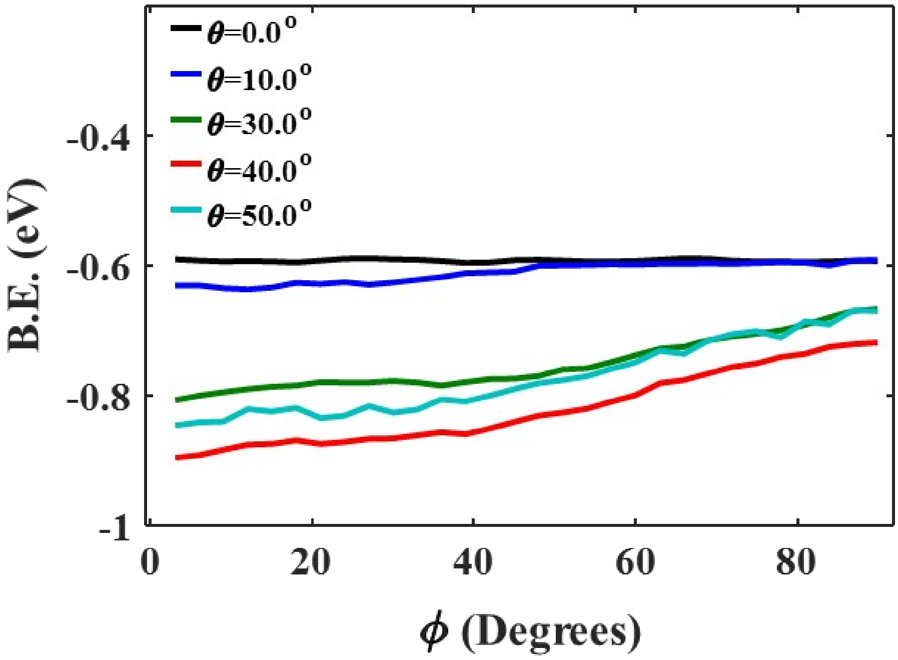

Figure S16. Binding energy of compound **1** onto a gold substrate as a function of the azimuthal angle *ϕ* and the tilt angle *θ*, (vdW).

E.6. Binding energy as a function of distance (*d*).

After tilting the molecule to the optimum values of *ϕ* (= 0°) and *θ* (in the 29-42° range), we now re-calculate the optimum distance between the anchor group and the gold substrate, Figure S11. This distance is angle dependent, because the amine group sterically hinders the binding when $\theta = 0°$ and therefore one expects the optimum binding distance to decrease at finite *θ*. This is confirmed by the red curve of Figure S17, which shows that the equilibrium distance decreases from 3.4 to 3.0 Å. Furthermore, the binding energy increases from approximately 0.6 to 0.8 eV.

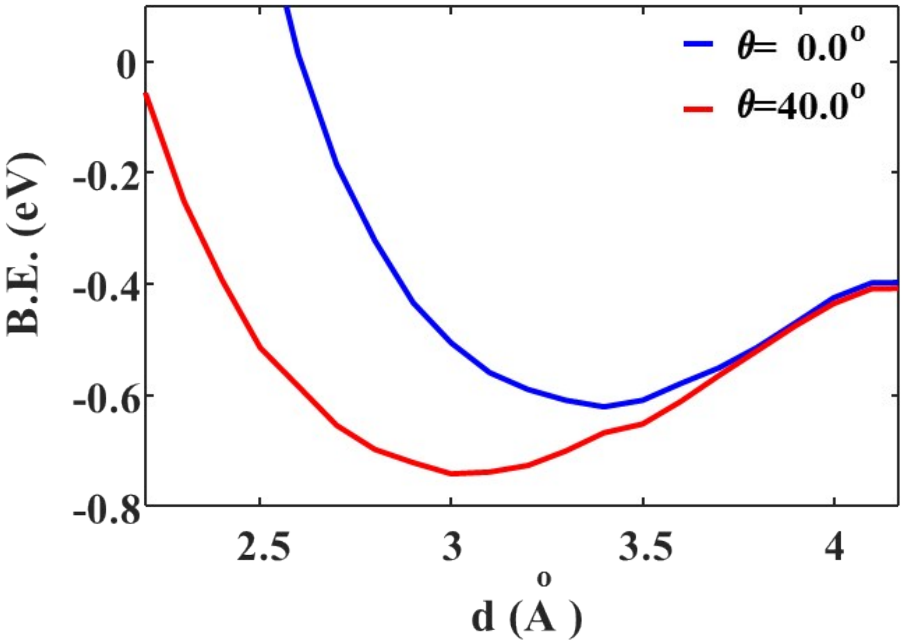

Figure S17. Binding energy as a function of the distance between the anchor group N and Au, (vdW).

This configuration is consistent with a double anchoring of compound 1 to the substrate by both the amine and the pyridine groups.

E.7. π-stacked molecular junction.

We now compare the properties of monomer and π-stacked dimer molecular junctions, as shown in Figure S18.

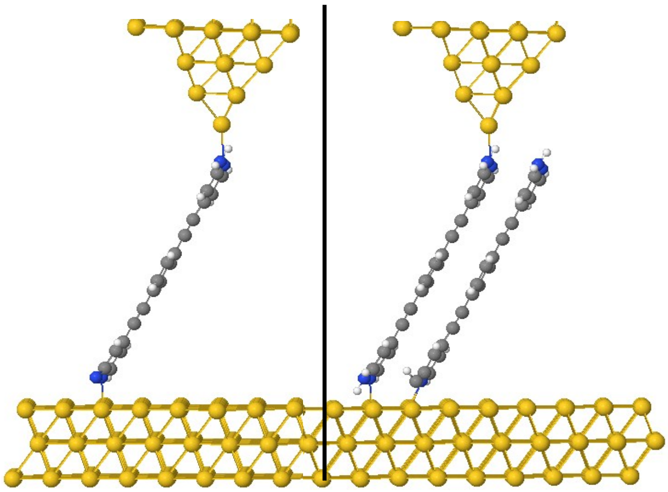

Figure S18. Cartoon illustrating a monomer and a dimer compound **1**-gold junction (left and right panel, respectively).

Figure S19 shows the total energy as a function of the dimer separation distance *D,* indicating that the optimum separation between the two molecules in the dimer is approximately 3.0 Å. Figure S20 shows the total energy as a function of the displacement *X*, and reveals that compound **1** prefers to slide relative each other up to the point where a N atom of one monomer is above the center of a terminal ring of the other. Figure S20 shows that their displacement, *X*, is approximately 1.4 Å.

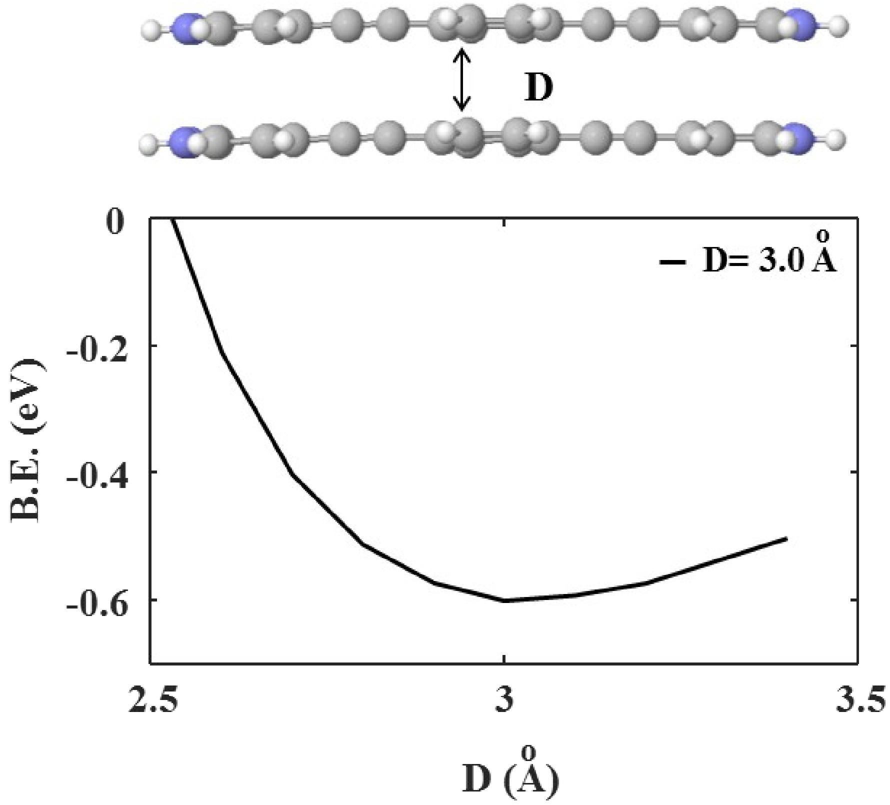

Figure S19. Binding energy as a function of the separation distance for compound **1** (vdW).

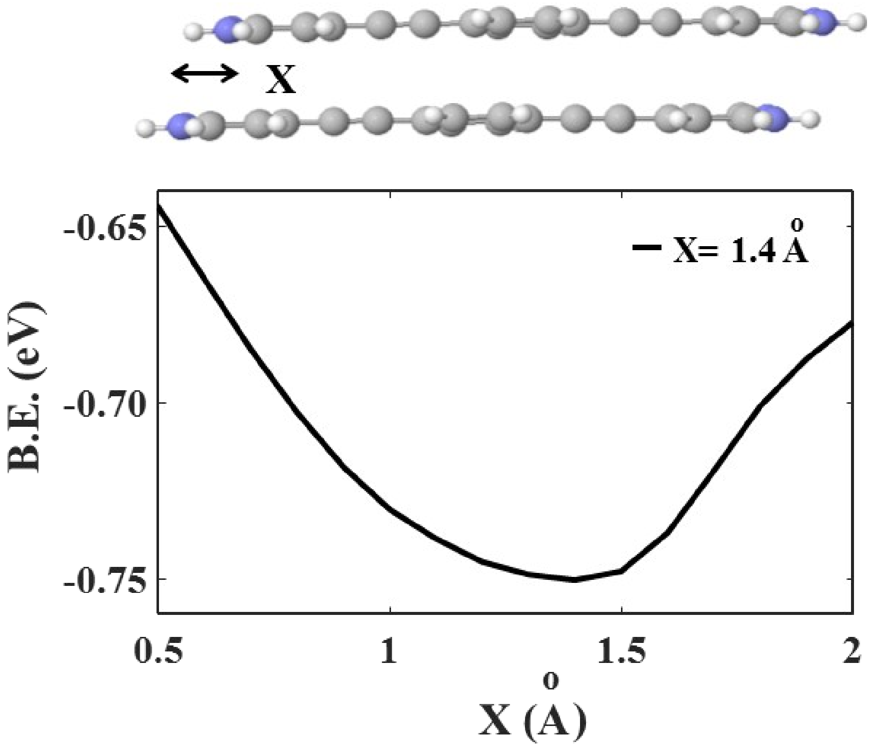

Figure S20. Binding energy as a function of the displacement distance *X* for compound **1,** (vdW).

E.8. HOMO-LUMO gap as a function of the separation distance and displacement distance.

Here, we calculate the HOMO-LUMO gap as a function of the separation distance *D* for the dimer (black line in Figure S21), and compare this value with the HOMO-LUMO gap for the monomer (red-circle in Figure S21). As shown in Figure S21 the HOMO-LUMO gap decreases when the separation distance decreases. The black curve shows that the gap value is independent of *D* at large distance (*D* > 5.0 Å). Figure S19 is indicative of an optimum separation distance of ca. 3.0 Å for which the HOMO-LUMO gap in the dimer corresponds to approximately a 1.5 eV gap (see the red dotted-lines). The red-circle represents the HOMO-LUMO gap for the monomer, which is larger than the gap dimer at the optimum distance. It is worth mentioning, that the displacement distance is zero (*X*=0 Å).

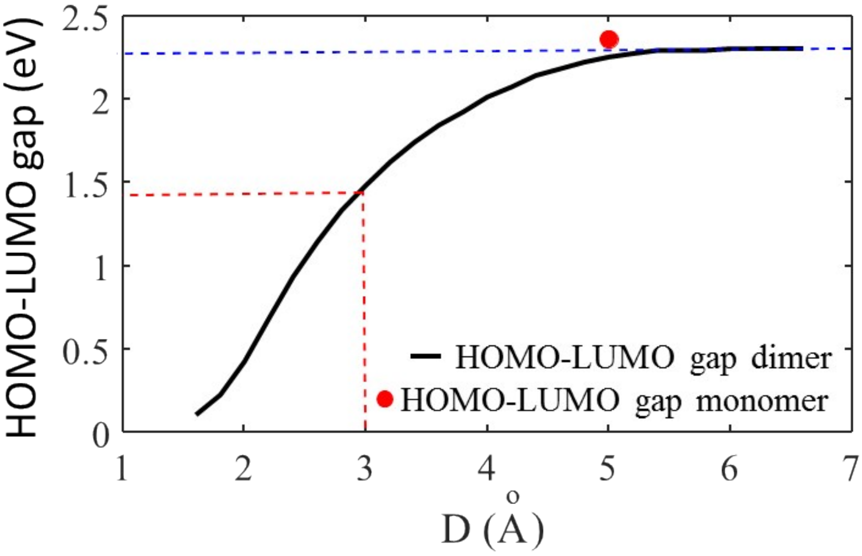

Figure S21. HOMO-LUMO gaps for monomer (red-circle), and dimer (black-curve) as a function of the separation distance *D*. The optimum separation is approximately 3.0 Å and that displacement distance is zero (*X*=0 Å).

Figure S20 indicates that the optimum displacement distance for the dimer is *X*=1.4 Å. Therefore to correct the calculated gaps in Figure S21, we recalculate the HOMO-LUMO gap as a function of the displacement distance with the optimum separation distance (*D*=3.0 Å). Figure S22 shows that the HOMO-LUMO gap increases with increasing *X* and the gap becomes independent of the displacement distance for $X > 2.0$ Å. The value of the HOMO-LUMO gap is approximately 2.1 eV at the optimum displacement (see the red dotted-lines). The HOMO-LUMO gap at the optimum *D* and *X* is 2.10 eV for the dimer and this value is lower than the one for monomer (red-circle). The calculated difference in gaps for dimer and monomer is in good agreement with the experimental measured difference in gaps (see Figure S24) where a red shift of the maximum absorption wavelength for the monolayer with respect to the solution can be observed, which is consistent with the formation of J-aggregates in the film.

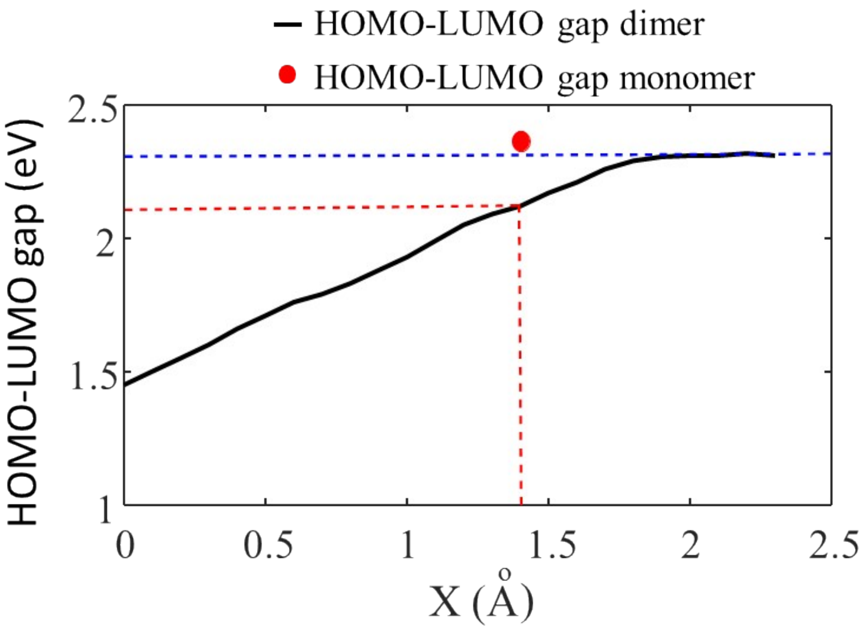

Figure S22. HOMO-LUMO gaps for monomer (red-circle), and dimer (black-curve) as a function of the displacement distance X.

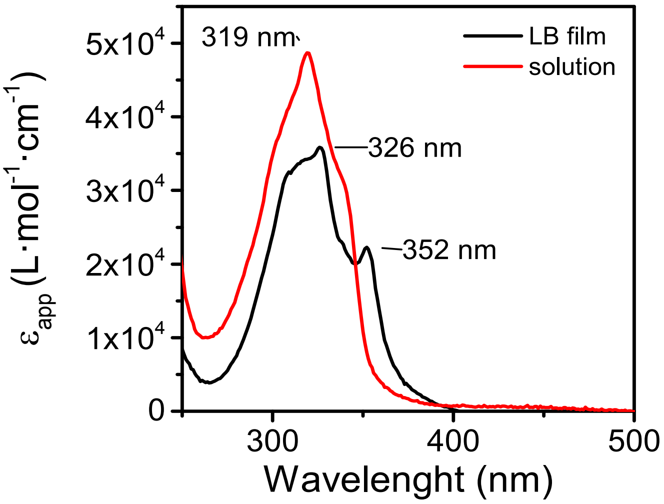

Figure S23. Apparent molar absorptivity[5] vs. wavelength for compound **1** in solution (DMSO:$CHCl_3$ 1:4) and for a LB monolayer of compound **1.**

E.9. Transmission coefficient as a function of energy for isomer-1 and isomer-2.

In this section, the transmission coefficient $T(E)$, for the *cis* and *trans* configurations (see Figure S12) is calculated. Figure S24 shows that the $T(E)$ curves of the two isomers are identical, and therefore in what follows we will focus on the transport properties of isomer 1 only.

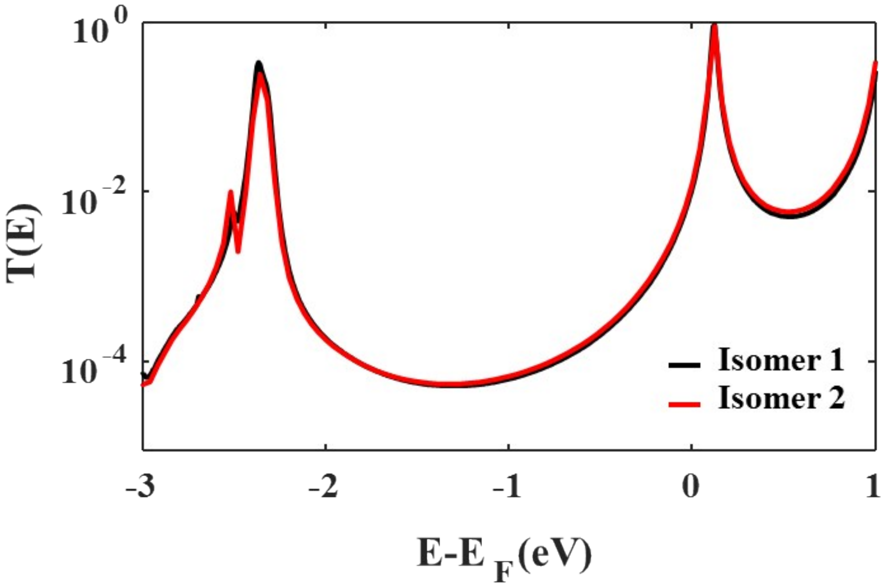

Figure S24. Zero base transmission coefficient as a function of energy of isomer 1 (black curve), and isomer 2 (red curve).

E.10. Binding energy as a function of LB monolayer.

We now examine the binding energy of a LB monolayer (Figure 25) film composed of 7 molecules.

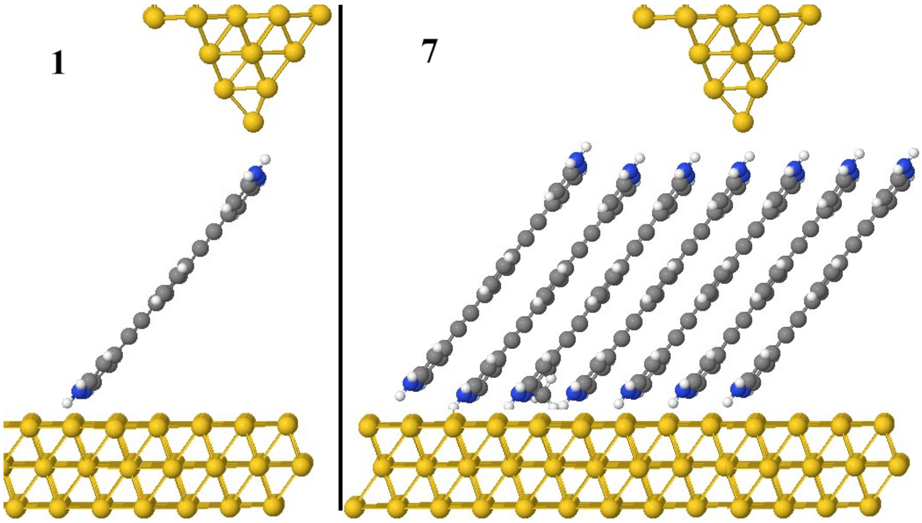

Figure S25. Cartoon illustrating a monomer (left) and LB monolayer (right) in a gold junction (left and right respectively).

Figure S26 shows the variation with the tilt angle of the total energy per molecule of the LB monolayer and that of a single-molecule junction. This plot shows that the most energetically favorable tilt angle of the LB monolayer (≈ 30°) is lower than that of the monomer (≈ 40°). These results are summarized in Table S1.

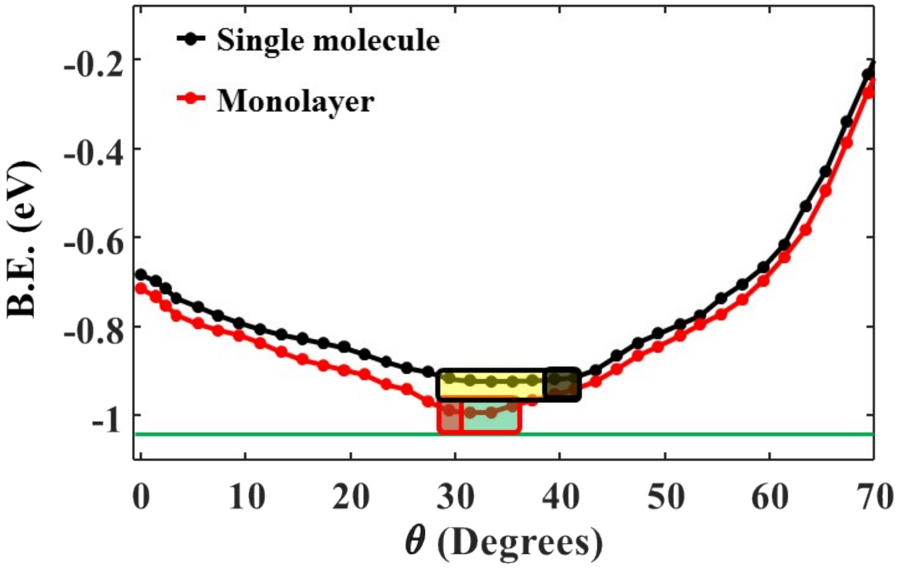

Figure S26. Binding energy as a function of the tilt angle for compound **1** (vdW). Binding energy calculations suggest the tilt angle for the LB monolayer to be approximately $\theta \approx$ 29.0-36.0° and experimental results suggest $\theta \approx$ 30.0°. The black squares and the red ones correspond to the experimental values for the single molecule and the monolayer, respectively.

Table S1: Comparison between experimental and calculated tilt angles for the single molecule and the monolayer.

Experimental Results	**Equivalent experimental tilt angle (*θ*)**	**Equivalent tilt angle (*θ*) as determined from the theoretical calculations**
Single molecule break-off distance 1.35 ± 0.1 nm	≈ 40°	29-42°
LB monolayer thickness 1.6 ± 0.1 nm	≈ 30°	29-36°

E.11. Binding energy as a function of tip position.

In this section, we will determine the most energetically favorable position for the pyramidal tip by placing the tip in 300 positions over the LB monolayer, as shown in the top panel of Figure S27. The energy minima in the bottom panel show that the tip prefers to position itself on the top of the pyridine-N atom. Based on this result, we next compute the transmission coefficients when the tip is in contact with the terminal pyridine-N atom.

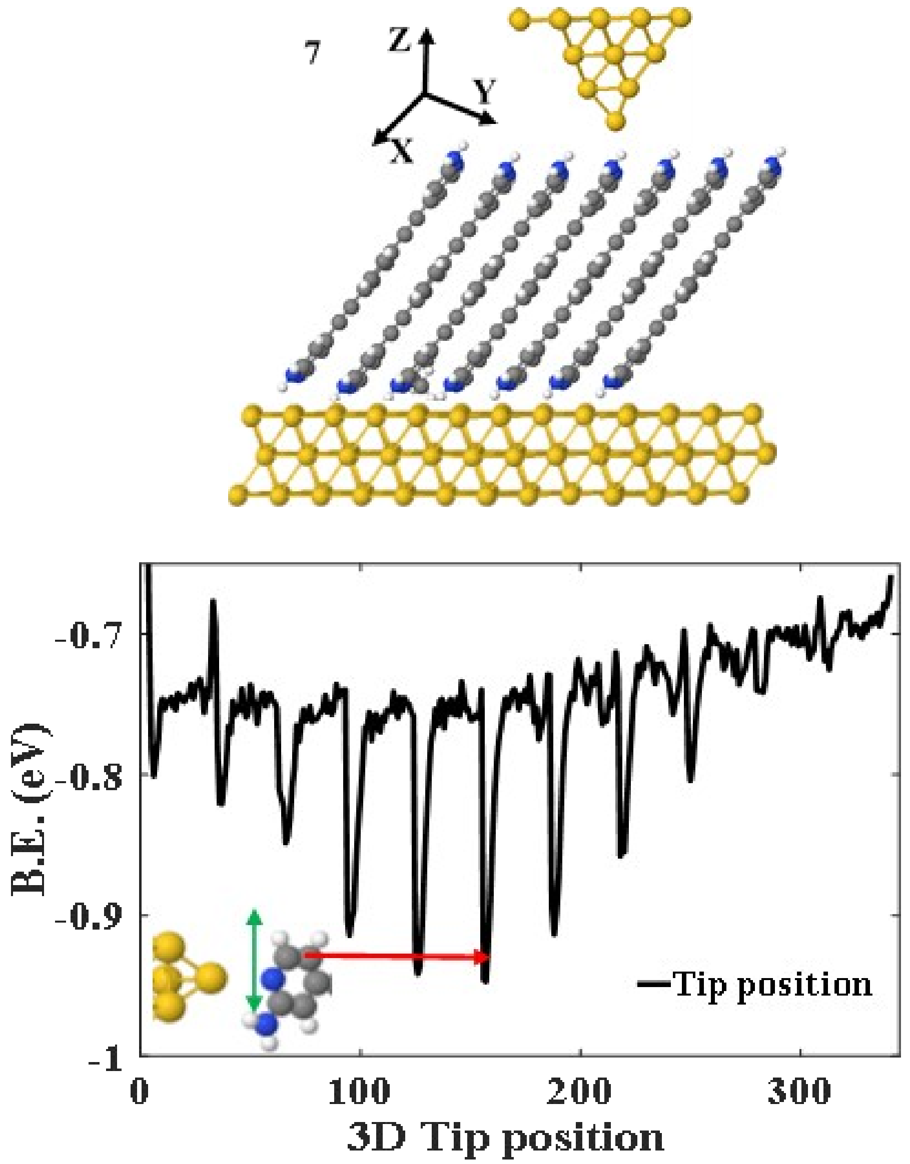

Figure S27. Binding energy as a function of the tip position onto the LB monolayer of compound **1,** (vdW). Binding energy calculations suggest that the tip prefers to bind to the pyridine-N atom (red arrow, bottom panel).

E.12. Transmission coefficient as a function of energy.

Figure S28 shows the transmission coefficients $T(E)$ of the monomer and dimer shown in Figure S18, and reveals that over a range of energies within the HOMO-LUMO gap, $T(E)$ of the monomer is slightly higher than that of the dimer. In these calculations, the tilt angles θ of the monomer and dimer are chosen to correspond to the measured break-off distance and to the monolayer thickness (see Figures S9 and S5 respectively and Table S1) and the calculated tilt angle (see Figure S26).

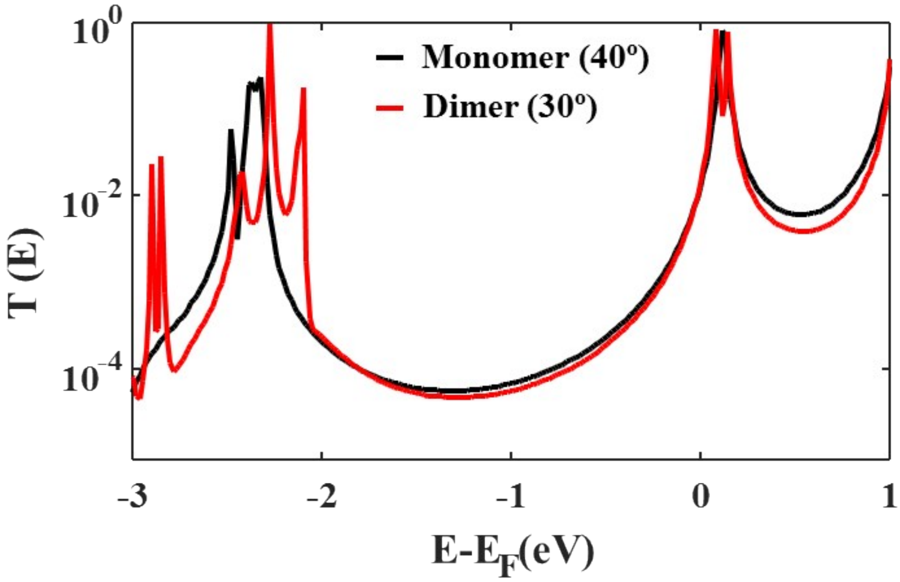

Figure S28. Zero bias transmission coefficient as a function of energy for the monomer (black curve) and dimer (red curve).

The transmission coefficients in Figure S28 correspond to junctions with a flat substrate and a pyramidal tip (see Figure S18). Since the shape of the top contact is not known, we also computed the transmission coefficient of a junction with a flat substrate and a flat top electrode (flat-flat). Figure S29 shows that the conductance of flat-flat junction is slightly higher than flat-tip junction, with the ratio between monomer and dimer transmission coefficients remaining approximately the same. This result seems to indicate that in a flat-flat configuration a double anchoring between the top contact electrode and compound **1** is favored resulting in a slight increase of the conductance.

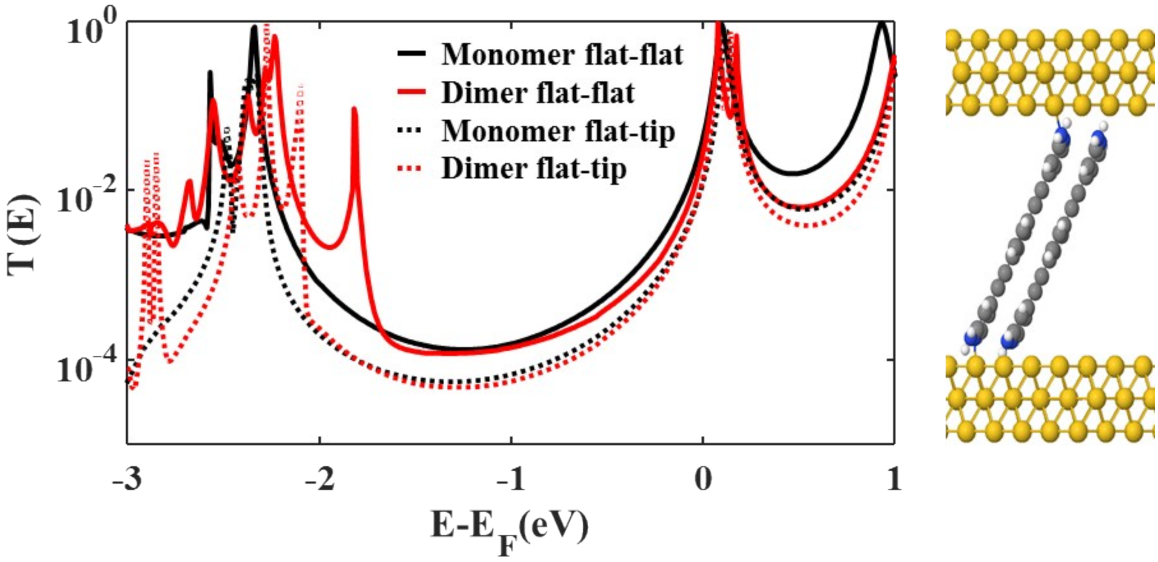

Figure S29. Zero bias transmission coefficients as a function of electron energy for a flat-flat junction (solid-lines), and a flat-tip junction (dotted-lines).

E.13. Monolayer vs dimer tranmissions.

Figure S30 shows that the $T(E)$ curve of the dimer is close to that of a monolayer containing a larger number of molecules. For this reason, the main electronic properties per molecule of a monolayer can be obtained simply by computing the transmission function of a dimer.

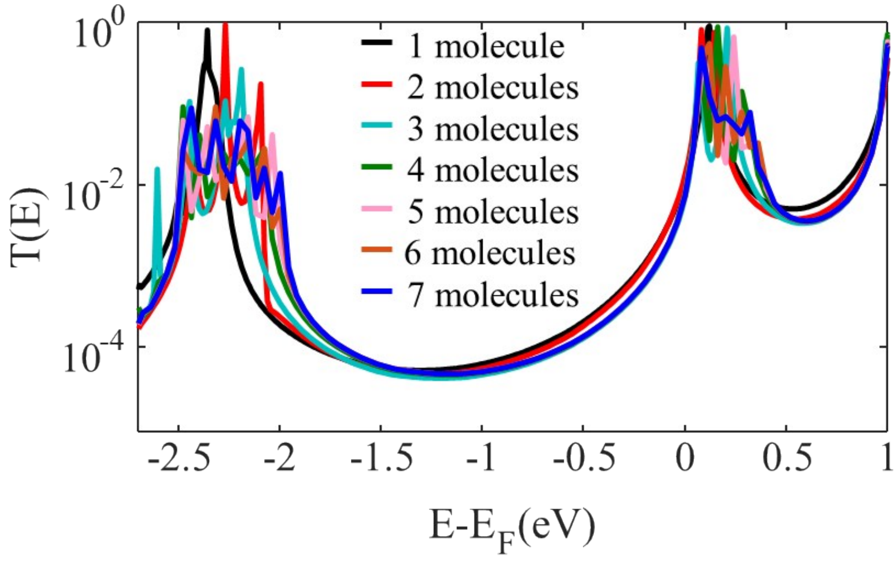

Figure S30. Zero base transmission coefficient as a function of energy for the indicated number of molecules onto gold.

F. Comparison of conductance values of OPE derivatives with different anchoring groups

It is often informative to compare the conductance values with those of related compounds but this is not necessarily straightforward if they are not part of a homologous chemical series. This is because molecular conductance has a number of complex and often-interrelated contributions. These may include contributions from the contacting electrode material, the surface contacting group,[6] the orientation and conformation of the molecule within the junction,[7,8] the solvent[9,10] and any electrolyte in the solvent environment,[11] as well as, of course, the chemical structure of the molecular backbone.[12] In addition, the morphology and surface roughness of the contacting material,[13] which themselves may be dependent on the nature of the method used to form the junction.[7,14] Added to this the conductance mechanism may change with molecular length, for example there may be a length-dependent transition from tunneling to hopping.[15-17] Comparisons of the conductance of molecules with similar chemical compositions but different connectivities or structures may be further impacted by quantum interference (QI). It is noted here that QI can have a very significant impact on the overall junction conductance.[18]

Table S2 collects together experimental conductance values obtained for a number of similar molecular materials, which for purpose of comparison have a single anchor groups or a double anchor groups. It seems that the double anchor results in higher conductance values, although further systematic studies are needed to fully understand the mechanism behind the experimental results.

Table S2. Reported conductance for similar compounds as single molecules or in monolayers (either Langmuir-Blodgett of Self Assembled films).

Molecule	Single molecule (G_o) and method	Monolayer (G_o)
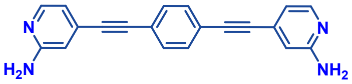	$1.2\cdot10^{-4}$ *I(s)*	$0.6\cdot10^{-4}$

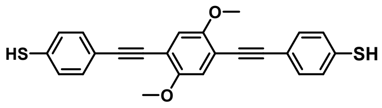	$2.0\cdot10^{-5}$ (7) *I(s)*	-
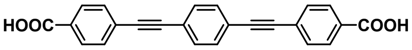	$1.8\cdot10^{-5}$ (8) *I(s)*	$0.3\cdot10^{-5}$ (8) $1.8\cdot10^{-5}$ (8)
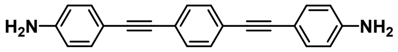	$2.4\cdot10^{-5}$ (9) *I(s)*	-
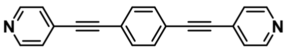	$5.4\cdot10^{-5}$ (19) *I(s)*	$5.2\cdot10^{-5}$ (19)
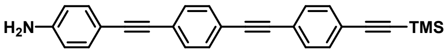	$2.4\cdot10^{-5}$ (20) *I(s)*	$1.2\cdot10^{-5}$ (11)
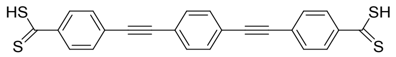	$2.5\cdot10^{-3}$ (21) *BJ*	-
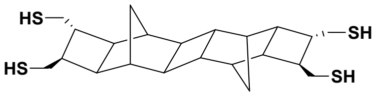	$3.5\pm1.2\cdot10^{-5}$ (22) *BJ*	
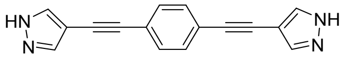	$3.4\cdot10^{-4}$ $2.4\cdot10^{-4}$ (23) *I(s)*	-

G. References

(1) Fortgang, P.; Tite, T.; Barnier, V.; Zehani, N.; Maddi, C.; Lagarde, F.; Loir, A.-S.; Jaffrezic-Renault, N.; Donnet, C.; Barrelie, F.et al. *Robust electrografting on self-organized 3D graphene electrodes*. ACS Appl. Mater. Interfaces, **2016**, *8*, 1424-1433.

(2) Bain, C. D.; Whitesides, G. M. *Attenuation lengths of photoelectrons in hydrocarbon films*. J. Phys. Chem., **1989**, *93*, 1670-1673.

(3) Nichols, R. J.; Haiss, W.; Higgins, S. J.; Leary, E.; Martin, S.; Bethell, D. *The experimental determination of the conductance of single molecules*. Phys. Chem. Chem. Phys., **2010**, *12*, 2801-2815.

(4) Bosh-Navarro, C.; Laker, Z. P.; Rourke, J. P.; Wilson, N. R. *Reproducible, stable and fast electrochemical activity from easy to make graphene on copper electrodes*. Phys. Chem. Chem. Phys., **2015**, *17*, 29628-29636.

(5) Cea, P.; Martín, S.; Villares, A.; Möbius, D.; López, M. C. *Use of UV-vis reflection spectroscopy for determining the organization of viologen and viologen tetracyanoquinodimethanide monolayers*. J. Phys. Chem. B, **2006**, *110* 963-970.

(6) Lhenry, S.; Leroux, Y.; Hapiot, P. *Use of catechol as selective redox mediator in scanning electrochemical microscopy investigations*. Anal. Chem., **2012**, *84*, 7518-7524.

(7) Martin, S.; Grace, I.; Bryce, M. R.; Wang, C. S.; Jitchati, R.; Batsanov, A. S.; Higgins, S.; Lambert, C. J.; Nichols, R. J. *Identifying diversity in nanoscale electrical break junctions*. J. Am. Chem. Soc., **2010**, *132*, 9157-9164.

(8) Ballesteros, L. M.; Martín, S.; Cortés, J.; Marqués-González, S.; Higgins, S. J.; Nichols, R. J.; Low, P. J.; Cea, P. *Controlling the structural and electrical properties of diacid oligo(phenylene ethynylene) Langmuir-Blodgett films*. Chem. Eur. J., **2013**, *19*, 5352-5363.

(9) Ferradás, R. R.; Marqués-González, S.; Osorio, H. M.; Ferrer, J.; Cea, P.; Milan, D. C.; Vezzoli, A.; Higgins, S. J.; Nichols, R. J.; Low, P. J.et al. *Low variability of single-molecule conductance assisted by bulky metal-molecule contacts*. RSC Adv., **2016**, *6*, 75111-75121.

(10) Osorio, H. M.; Martin, S.; Carmen Lopez, M.; Marques-Gonzalez, S.; Higgins, S. J.; Nichols, R. J.; Low, P. J.; Cea, P. *Electrical characterization of single molecule and Langmuir-Blodgett monomolecular films of a pyridine-terminated oligo(phenylene-ethynylene) derivative*. Beilstein J. Nanotechnol., **2015**, *6*, 1145-1157.

(11) Pera, G.; Martín, S.; Ballesteros, L. M.; Hope, A. J.; Low, P. J.; Nichols, R. J.; Cea, P. *Metal-molecule-metal junctions in Langmuir-Blodgett films using a new linker: trimethylsilane*. Chem. Eur. J., **2010**, *16*, 13398-13405.

(12) Xiang, D.; Wang, X.; Jia, C.; Lee, T.; Guo, X. *Molecular-scale electronics: from concept to function*. Chem. Rev., **2016**, *116*, 4318-4440.

(13) Kotulska, M.; Kubica, K. *Structural and energetic model of the mechanisms for reduced self-diffusion in a lipid bilayer with increasing ionic strength*. Phys. Rev. E: Stat., Nonlinear, Soft Matter Phys., **2005**, *72*, 061903.

(14) Haiss, W.; Martin, S.; Leary, E.; van Zalinge, H.; Higgins, S. J.; Bouffier, L.; Nichols, R. J. *Impact of junction formation method and surface roughness on single molecule conductance*. J. Phys. Chem. C., **2009**, *113*, 5823-5833.

(15) Luo, L.; Choi, S. H.; Frisbie, C. D. *Probing Hopping Conduction in Conjugated MolecularWires Connected to Metal Electrodes*. Chem. Mater., **2011**, *23*, 631-645.

(16) Vilan, A.; Aswal, D.; Cahen, D. *Large-area, ensemble molecular electronics: motivation and challenges*. Chem. Rev., **2017**, *117*, 4248-4286.

(17) Lu, Q.; Liu, K.; Zhang, H.; Du, Z.; Wang, X.; Wang, F. *From tunneling to hopping: a comprehensive investigation of charge transport mechanism in molecular junctions based on oligo(p-phenylene ethynylene)s*. ACS Nano, **2009**, *3*, 3861-3868.

(18) Maity, P.; Takano, S.; Yamazoe, S.; Wakabayashi, T.; Tsukuda, T. *Binding motif of terminal alkynes on gold clusters*. J. Am. Chem. Soc., **2013**, *135*, 9450-9457.

(19) Osorio, H. M.; Martín, S.; López, M. C.; Marqués-González, S.; Higgins, S. J.; Nichols, R. J.; Low, P. J.; Cea, P. *Electrical characterization of single molecule and Langmuir–Blodgett monomolecular films of a pyridine-terminated oligo(phenylene-ethynylene) derivative*. Beilstein J. Nanotechnol., **2015**, 1145-1157.

(20) Fatemi, V.; Kamenetska, M.; Neaton, J. B.; Venkataraman, L. *Environmental Control of Single-Molecule Junction Transport*. Nano Lett., **2011**, *11*, 1988-1992.

(21) Xing, Y.; Park, T. H.; Venkatramani, R.; Keinan, S.; Beratan, D. N.; Therien, M. J.; Borguet, E. *Optimizing single-molecule conductivity of conjugated organic oligomers with carbodithioate linkers*. J. Am. Chem. Soc. , **2010**, *132*, 7946-7956.

(22) Darwish, N.; Aragones, A. C.; Darwish, T.; Ciampi, S.; Diez-Perez, I. *Multi-responsive photo- and chemo-electrical single-molecule switches*. Nano Letters, **2014**, *14*, 7064-7070.

(23) Matyszewska, D.; Bilewicz, R.; Su, Z.; Abbasi, F.; Leitch, J. J.; Lipkowski, J. *PM-IRRAS studies of DMPC bilayers supported on Au(111) electrodes modified with hydrophilic monolayers of thioglucose*. Langmuir, **2016**, *32*, 1791-1798.